

Article

Combustion Characterization in a Diffusive Gas Turbine Burner for Hydrogen-Compliant Applications

Salvatore Carusotto ¹, Prashant Goel ¹, Mirko Baratta ^{1,*}, Daniela Anna Misul ^{1,*}, Simone Salvadori ¹,
Francesco Cardile ², Luca Forno ², Marco Toppino ² and Massimo Valsania ²

¹ Dipartimento Energia DENERG, Politecnico di Torino, Corso Duca degli Abruzzi 24, 10129 Torino, Italy; salvatore.carusotto@studenti.polito.it (S.C.); prashant.goel@polito.it (P.G.); simone.salvadori@polito.it (S.S.)

² Ethos Energy Italia S.p.A., Corso Romania 661, 10156 Torino, Italy; francesco.cardile@ethosenergygroup.com (F.C.); luca.forno@ethosenergygroup.com (L.F.); marco.toppino@ethosenergygroup.com (M.T.); massimo.valsania@ethosenergygroup.com (M.V.)

* Correspondence: mirko.baratta@polito.it (M.B.); daniela.misul@polito.it (D.A.M.)

Abstract: The target of net-zero emissions set by the 2015 Paris Agreement has strongly commissioned the energy production sector to promote decarbonization, renewable sources exploitation, and systems efficiency. In this framework, the utilization of hydrogen as a long-term energy carrier has great potential. This paper is concerned with the combustion characterization in a non-premixed gas turbine burner, originally designed for natural gas, when it is fed with NG-H₂ blends featuring hydrogen content from 0 to 50% in volume. The final aim is to retrofit a 40 MW gas turbine. Starting from the operational data of the engine, a CFD model of the steady-state combustion process has been developed, with reference to the base load NG conditions, by reducing the fuel mass-flow rate by up to 17% to target the baseline turbine inlet temperature. When the fuel is blended with hydrogen, for a given temperature at turbine inlet, an increase in the peak temperature up to 800 K is obtained, if no countermeasures are taken. Furthermore, the flame results are more intense and closer to the injector in the case of hydrogen blending. The results of this work hint at the necessity of carefully analyzing the possible NO_x compensation strategies, as well as the increased thermal stresses on the injector.

Keywords: hydrogen; CFD; non-premixed combustion; retrofitting; gas turbines



Citation: Carusotto, S.; Goel, P.; Baratta, M.; Misul, D.A.; Salvadori, S.; Cardile, F.; Forno, L.; Toppino, M.; Valsania, M. Combustion Characterization in a Diffusive Gas Turbine Burner for Hydrogen-Compliant Applications. *Energies* **2022**, *15*, 4117. <https://doi.org/10.3390/en15114117>

Academic Editors: Raffaele Tuccillo and Fabrizio Reale

Received: 15 May 2022

Accepted: 31 May 2022

Published: 3 June 2022

Publisher's Note: MDPI stays neutral with regard to jurisdictional claims in published maps and institutional affiliations.



Copyright: © 2022 by the authors. Licensee MDPI, Basel, Switzerland. This article is an open access article distributed under the terms and conditions of the Creative Commons Attribution (CC BY) license (<https://creativecommons.org/licenses/by/4.0/>).

1. Introduction

To achieve the goals of the 2015 Paris Agreement, clean energy transition is required to result in a rapid reduction in the emission of greenhouse gases to zero on a net basis over the coming decades. More specifically, the increase in the global average temperature should be maintained at a much lower level than 2 °C, and efforts should be focused on limiting the temperature increase to 1.5 °C above pre-industrial levels. The ambitious target of net-zero CO₂ emissions for the energy sector indicates that emissions persisting from specific world areas or from sectors where abatement is technically difficult or not economically sustainable have to be compensated through carbon capture and storage in other parts of the energy sector [1]. These results constitute a real challenge for the industry and research sectors and can only be achieved if a proper mix of alternative fuels and breakthrough technologies will be found.

With specific reference to the power generation sector, gas turbines are forecasted to maintain their important contribution, essentially due to their capability to be complementary to the non-programmable fluctuation of renewable energy sources. Gas turbine cycles have reached remarkable efficiency levels, especially when combined with steam turbines in combined cycle plants (CCP) or cogeneration. Concerning the development pathways, two directions can be identified:

- i. Cycle optimization using pressure-gain combustion [2,3], involving secondary flows and blade cooling [4];

ii. development of fuel-flexible combustion systems [5–7].

Notably, the latter pathway is not only oriented to developing new gas turbine engines, but also has great potential in retrofitting existing turbines. Extending the lifetime of power generation plants is a significant step toward sustainability [8,9]. With specific reference to the fuel-flexible capability of gas turbine combustors, it can lead to different benefits. On the one hand, the exploitation of biogases can be allowed, through maintaining an acceptable combustion stability and guaranteeing robustness to autoignition and flash-back [5]. On the other hand, the possibility of running the engines on hydrogen or natural gas (NG)-hydrogen blends can be considered. The latter can promote a significant increase in the exploitation capability of the intrinsically fluctuating, renewable energy sources (RES), thanks to its great potential to store large amounts of the excess electricity [1].

Several studies have been proposed over the years to address the possibility of burning hydrogen in gas turbines, whether developed on purpose or originally designed to run on natural gas. At a cycle level, hydrogen can be used as gas turbine fuel with limited efficiency reduction if the peak temperature is reduced using steam or nitrogen [10]. The effects of hydrogen addition on the pollutant emissions of an unconfined swirling flame are studied using computational fluid dynamics (CFD) on a simplified geometry [11]. The authors demonstrate that, by increasing the volumetric hydrogen percentage, the size of the maximum temperature region is reduced, while the temperature peak increases as well as the NO_x emissions. Notably, for low volumetric hydrogen percentage (less than 10%), the combustion characteristics of the flame are mostly unchanged. In another research activity, large-eddy simulation is performed on a DLR burner to investigate emissions of a methane-hydrogen blend [12]. Herein, it is confirmed that even though the addition of hydrogen promotes a reduction in the flame length, a curtailed concentration of hydrogen is responsible for an enhanced flame length (similar to the one associated with pure methane) since for low volumetric hydrogen concentrations the lateral size of the mixing region is reduced.

To date, hydrogen-fired gas turbines are beyond the demonstration level [1], while several issues persist regarding the availability of hydrogen, the process used for its production, and its integration with the turbine working cycle. Concerning its availability and production, it is possible to generate hydrogen using green energy (from solar power plants or wind turbines) or mixed sources. The first solution is preferable since it provides the so-called ‘green hydrogen’ that acts as energy storage and allows for balancing the energy grid and maximizing the RES exploitation. These factors can lead to the highest possible emissions reduction [13]. From a technological point of view, the main problem associated with hydrogen combustion in non-premixed flames is the generation of high-temperature regions, where NO_x will likely be formed in quantities above the allowed limitations. Switching to premixed combustion would ease the reduction of NO_x emissions. However, the high hydrogen flame speed may be responsible for flashbacks, thus reducing combustor reliability [10,14]. As a result, it is not possible to individuate a straightforward way to implement hydrogen combustion in gas turbine. However, in the lifetime extension field, a non-premixed approach is more probable due to the characteristics of the original combustors (most of them developed in the mid-1980s), while a premixed approach is preferable when combustors are designed for new gas turbines. In a pioneering work on the redesign of heavy-duty gas turbines to operate at 100% hydrogen fuel at reduced NO_x production, CFD is successfully used to design new injection systems for a 10 MW gas turbine combustion chamber [15]. In successive research, CFD is used to support an experimental campaign performed on an atmospheric combustion test facility to develop and test a lean premixed burner prototype aimed at identifying some practical data for use in the development of low-NO_x hydrogen burner, which is suitable for heavy-duty gas turbine [16]. In this case, the internal recirculation zone was reinforced by means of a new swirler and a movable fuel injection system together with a removable ogive were installed at the exit, both allowing for the control of the flame flash-back phenomena.

Further literature contributions on hydrogen combustion in gas turbines for stationary applications can be found in [7,17–20].

This paper presents the results of a research activity carried out at Politecnico di Torino in collaboration with EthosEnergy Italia Spa, aimed at retrofitting the combustor of a 40 MW turbine to allow for the operation of blends of compressed natural gas (CNG) and hydrogen (HCNG) with hydrogen content up to 50% in volume. The development of retrofit solutions for existing gas turbines is expected to provide a significant boost to the implementation of the hydrogen gas turbine technology, as well as ensuring advantages in terms of production costs, product reliability, and readiness of the solution [9]. Therefore, a thorough investigation of the combustion characteristics for different hydrogen blending, under non-premixed conditions is presented. In the first section of the paper, combustor and fuel characteristics are reported. The numerical model is discussed in the second section, with special attention to grid dependence analysis and to the impact of the Schmidt number value on the numerical diffusivity. Then, the results are discussed for the selected NG-H₂ blends in terms of temperature and velocity fields inside of the combustor. The outlet temperature profile is also discussed, as well as combustion characteristics through OH maps. Finally, the obtained results are used to individuate possible strategies for design modifications aimed at improving the performance of the gas turbine with hydrogen blends.

2. Turbine under Investigation

The present study is focused on the TG20 B7/8 turbine, which belongs to the EthosEnergy portfolio, and has already been the focus of two published works by the authors [4,21]. A section of the turbine through the axis is reported in Figure 1.

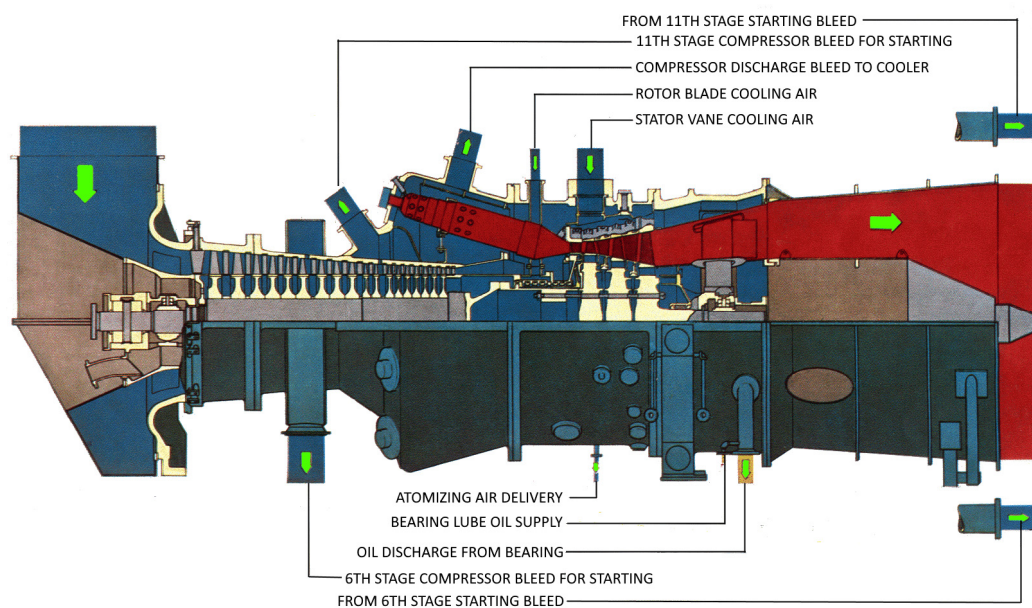


Figure 1. Turbine section along the axis. Green arrows indicate the gas primary and secondary-flow direction.

The air at the compressor delivery is partially used to feed the bleedings toward the turbine cooling secondary circuit. Downstream of the flow split, the majority of the air is directed to eight tubular, non-premixed combustors. Downstream of the combustors, eight transition pieces (TPs) deliver the hot exhaust gases to the turbine stages, and finally to a discharge diffuser.

The geometry of the combustor under study is provided in Figure 2, along with the indication of its main connections with the other components.

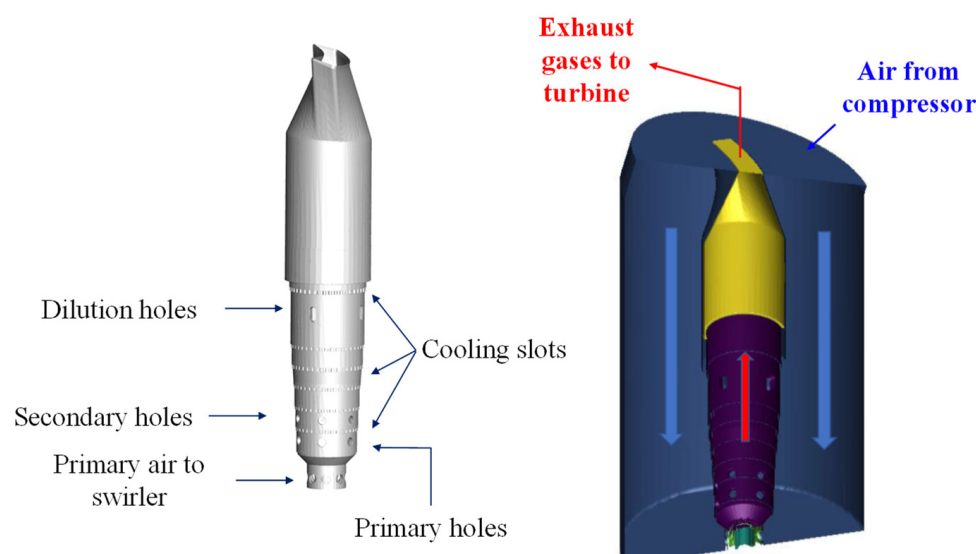


Figure 2. Tubular combustor geometry and main connections.

The left image in the figure is relative to the surface of the combustion basket and the TP. Moreover, the path of the oxidizing, dilution, and cooling air can be understood from the indication of the different holes in the basket shell. In the right picture, the blue and red arrows highlight the compressed path of air and exhaust gases, respectively. Furthermore, the volume of the external casing is represented, as it has been modeled in the CFD simulations described below.

The results presented in this paper are obtained by a series of comparative simulations, for different NG-H₂ blends. The main properties of the fuel blends (formula, stoichiometric air-to-fuel ratio, $(A/F)_{st}$, LHV) are reported in Table 1.

Table 1. Fuel blends properties.

H ₂ Vol. Fraction [%vol]	Short Formula	$(A/F)_{st}$ [-]	LHV [MJ/kg]
0 (Base Load)	C _{1.21} H _{4.02} O _{0.19}	11.3	41.6
15	C _{1.03} H _{3.71} O _{0.16}	11.6	43.3
25	C _{0.91} H _{3.51} O _{0.14}	11.9	44.7
50	C _{0.60} H _{3.01} O _{0.10}	13.0	50.3

The base load with pure NG was characterized by taking the reference fuel data at EthosEnergy. The rather low values of $(A/F)_{st}$ and LHV are to be ascribed to a non-negligible CO₂ content in the fuel mixture. Nevertheless, since no precise data could be considered for the hydrogen composition, given the variety of solutions that can be considered for its supply chain, it was decided to blend the ‘real’ NG with pure hydrogen, the latter being characterized by $(A/F)_{st} = 34$ and LHV = 120 MJ/kg.

The simulation parameters were defined starting from the base load case and by targeting the same temperature at turbine inlet (TIT). By neglecting the effect of the fuel composition on the ratio of specific heats of the exhaust gases, which appears to be reasonable for hydrogen volume fractions up to 50% (corresponding to around 11% in mass), and by considering a fixed corrected speed for the compressor, a constant air mass-flow rate can be assumed. Consistently, the same compression delivery pressure and temperature can be postulated as a starting point for the analysis presented in this work. As a further development stage, a closer focus will be required for an in-depth investigation of any modification in the matching between compressor and turbine, due to the changes in the volumetric flow rate and the adiabatic index of exhaust gases [10].

3. Numerical Model Description

The numerical analysis has been performed employing a commercial software (CONVERGE 3.0, licensed from Convergent Science) and addressed the entire combustor geometry, including both the basket and the transition piece (TP). Moreover, the casing surrounding the combustion basket has been included in the computational domain. Furthermore, the mass-flow rate of the cooling slots was part of the problem solution, which is a peculiar feature with respect to the other studies in the literature, to the best of the authors' knowledge. While the primary, secondary, and dilution flows are included in the solution [7,22] or imposed as boundary conditions, the mass-flow rate of the cooling slots is often modeled by means of an approximated solution involving porous walls. However, this solution might be slightly questionable unless experimental or calculated data are available for the calibration of the porous medium parameters. An example where the cooling slots are part of the computational domain is given by [23], although the overall computational model was sufficiently small to avoid an excessive cell count.

3.1. Numerical Method

The computational effort could not be financially afforded if the complete geometry of an industrial case study was modeled. For this reason, the Reynolds averaged Navier-Stokes equations (RANS) were set as governing equations. In this first analysis, the attention was focused on the average combustor behavior, rather than the combustion instability, as the latter is a less stringent problem in non-premixed burners. Consequently, a steady-state approach could be adopted, thus reducing the overall computational cost. For this purpose, the pressure-implicit with splitting of operators (PISO) algorithm was selected together with a second-order upwind flux scheme for the momentum equation. Additional information on the convergence process will be provided in Section 3.2.

The boundary conditions were imposed starting from the data provided by EthosEnergy Italia S.p.A (Torino, Italy), in particular from the so-called 'base load' conditions, which represents the standard operating point for the turbine under investigation. The physical conditions imposed at the boundaries are reported in Table 2.

Table 2. Boundary conditions.

Location	Boundary Conditions
Casing Air Inflow	Compressor Mass-Flow Rate
Fuel Inflow	Fuel Mass-Flow Rate
Outflow	Pressure/Backflow Temperature
Walls	Adiabatic (Homogeneous Neumann)

To maintain the turbine inlet temperature (TIT) at a constant level among the several simulations, the injected fuel quantity has been adjusted in accordance with the different blends. The resulting fuel flow rate reduction referred to as the base load quantity is reported in Table 3. Additionally, based on full-engine field test results available at EthosEnergy, as well as on preliminary working cycle simulations, the heat transfer toward the surroundings was shown as negligible with respect to the overall chemical energy associated with the fuel flow. In particular, the assumption was not prejudicial for the prediction of the thermal field in the basket, thanks to the reproduction of the cold flow film generated by the cooling slots, as shown in Section 4. Therefore, the adjustments in the fuel mass-flow rate are a direct consequence of the modified fuel LHV (Table 1).

Concerning the grid, the CONVERGE built-in Cartesian grid has been employed with base dimensions of $(0.02 \times 0.02 \times 0.02)$ m together with fixed embedding and adaptive mesh refinement (AMR) for a total number of cells, which is equal to 9.9×10^6 .

Both fixed embedding and AMR contribute to the refinement of the base grid and are based on the following scaling equation:

$$dq_{ref} = \frac{dq_{base}}{2^n} \quad (1)$$

where dq_{base} is the base grid dimension, dq_{ref} is the refined grid dimension, and n is the ‘embedding scale’ set by the user.

Table 3. Normalized fuel mass-flow rates for CNG and the different HCNG blends.

H2 Vol. Fraction [%vol]	Fuel Mass-Flow Rate
0 (Base Load)	100%
15	96%
25	92.9%
50	82.6%

The fixed embedding strategy is applied in a fixed area of the domain with a defined embedding scale. Rather, the AMR is a peculiar embedding algorithm developed by CONVERGE and is used to control the mesh-induced numerical errors for a series of variables, such as temperature, velocity or turbulence quantities. The refinement is automatically activated when the estimation for the variable gradient reaches a threshold set by the user [24]. The use of AMR helps in reducing the fixed embedding scale and this is very helpful in an industrial application, where the geometry under investigation is complex.

The grid control details for this set of simulations are reported in Table 4.

Table 4. Grid control details.

Type	Location	Embedding Scale/Grid Size
AMR (Velocity)	Entire domain	3/2.5 mm
AMR (Temperature)	Entire domain	4/1.25 mm
Fixed Embedding	Combustor	2/5 mm
Fixed Embedding	Injection system	3/2.5 mm
Fixed Embedding	Head-end	2/5 mm
Fixed Embedding	Transition Piece	2/5 mm
Fixed Embedding	Swirler	5/0.625 mm
Fixed Embedding	Liner	2–3/5–2.5 mm
Fixed Embedding	Injectors Downstream	5/0.625 mm
Fixed Embedding	Injector Holes	7/0.156 mm

The present model has been developed starting from the results obtained by the authors in [25], where a non-premixed combustion CFD model was developed and validated. The validation results shown in [25], together with the grid-independence analysis and the Schmidt number sensitivity presented below, substantiate the accuracy and reliability of the CFD model used in this work.

3.2. Turbulence and Combustion Models

As previously stated, the current work is based on RANS simulations. This approach helps in maintaining low computational costs with an acceptable description of the main turbulence effects, with specific focus on its interaction with the combustion process. To model the turbulence, the k - ϵ re-normalization group (RNG) was used. The main difference with the standard k - ϵ was introduced in the energy dissipation equation, where an additional term is present [26].

$$\frac{\partial(\rho\epsilon)}{\partial t} + \frac{\partial(\rho u_i \epsilon)}{\partial x_i} = \frac{\partial}{\partial x_i} \left(\frac{\mu}{Pr} \cdot \frac{\partial \epsilon}{\partial x_j} \right) + C_{\epsilon 3} \rho \epsilon \frac{\partial u_i}{\partial x_i} + \left(C_{\epsilon 1} \frac{\partial u_i}{\partial x_j} \tau_{ij} - C_{\epsilon 2} + C_s S_s \right) \frac{\epsilon}{k} + S - \rho R \quad (2)$$

where

$$R = \frac{C_{\mu}\eta^3 \left(1 - \frac{\eta}{\eta_0}\right) \epsilon^2}{1 + \beta\eta^3} \frac{\epsilon^2}{k} \quad (3)$$

The k - ϵ RNG is widely used in the case of swirled flows, since it has been demonstrated that it generally guarantees a better agreement with experimental data [27]. In addition, it has been successfully employed for hydrogen combustion in gas turbine applications [6,28].

Concerning the combustion modeling, the flamelet-generated manifold (FGM) model developed by van Oijen, J.A. and de Goey, L.P.H. [29] was used. This model was used by the authors in [25] for a diffusive combustion from a bluff body. The model is based on the solution of a set of equations on the main combustion variables before the actual simulation takes place, thus generating the so-called ‘flamelet manifold’. The results of this procedure are used to create a 2D look-up table that is read during the simulation. Overall, the computational cost is reduced without significantly losing in terms of accuracy. After a few preliminary calculations, the initialization of the reactive simulation was optimized, to enhance the capability of the FGM model to converge to a stable solution. In detail, with reference to the region inside the liner, the initial temperature was set at a value close to the estimated adiabatic flame temperature and, at the same time, the progress variable was set to 1.

A summary of the case setup is reported in Table 5.

Table 5. Case setup overview.

Overview TG20 Setup	
Solver	Steady-state, PISO
Flux Scheme	Second-order upwind (MUSCL)
Turbulence Modeling	k- ϵ RNG
Combustion Modeling	FGM 1D diffusive
Reaction Mechanism	GRI-Mech 3.0

3.3. Numerical Model Convergence

Preliminary simulations were run in order to optimize the convergence of the model toward a stable, steady-state solution. Starting from the initial conditions corresponding to fluid at rest, the algorithm took around 5000 PISO cycles (corresponding to a time marching in ‘pseudo-time’) to reach a converged value for the mass-flow rate. The convergence was also facilitated by the adoption of a ‘grid scaling’ approach, which applied a reduction in the embedding scales by one level. This led to a doubled grid size in all the mesh regions, and in turn to (i) a lower temporal duration of each time step, and (ii) reduced numerical fluctuations in the initial calculation phase. The switch to the final grid size was set at 15 K cycles. Since then, the model did not reach a perfectly steady-state solution, rather, it showed a moderate fluctuation around an average value. For this reason, it was decided to extract a temporally-averaged solution between 20 and 30 K cycles, which was considered as representative of the burner behavior. This average was applied to both the 2D Cartesian charts and the variable contours, using the average functionality available in the CONVERGE package.

3.4. Grid Independence Analysis

The grid independence analysis has been performed preliminarily in this study case. In particular, to reduce the computational load in the refined case, the analysis has been carried out on a ‘reduced’ geometry without the transition piece. Two meshes were considered for the present analysis, which will be referred to as base and refined grid. The two grids are reported in Figure 3. Red lines are used to indicate the refined grid mesh lines, whereas the black lines refer to the base grid. The black color has been set with higher visualization priority, where the lines are overlapped. Consequently, when a red line is visible, this indicates that the grid size of the refined mesh is lower.

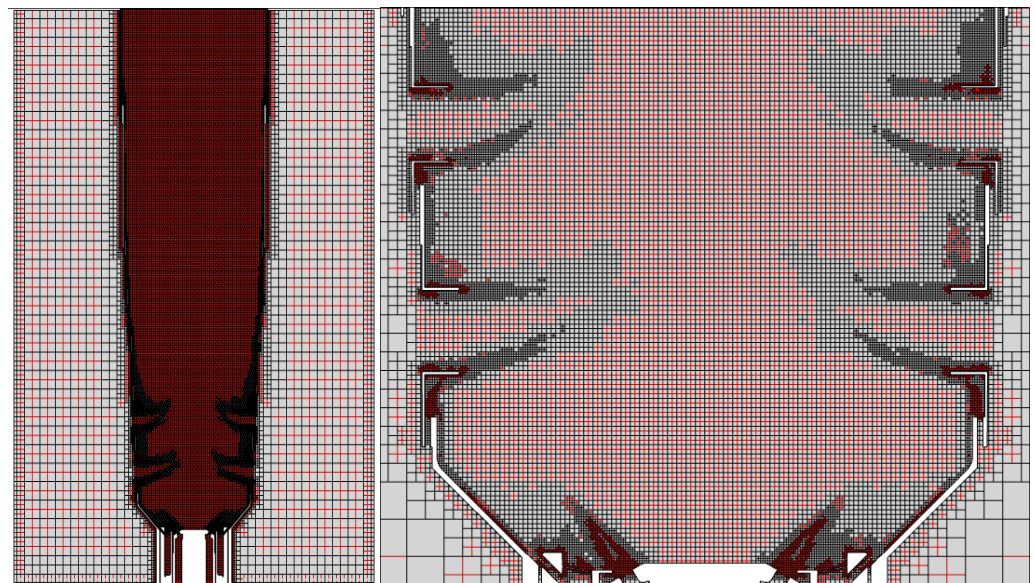
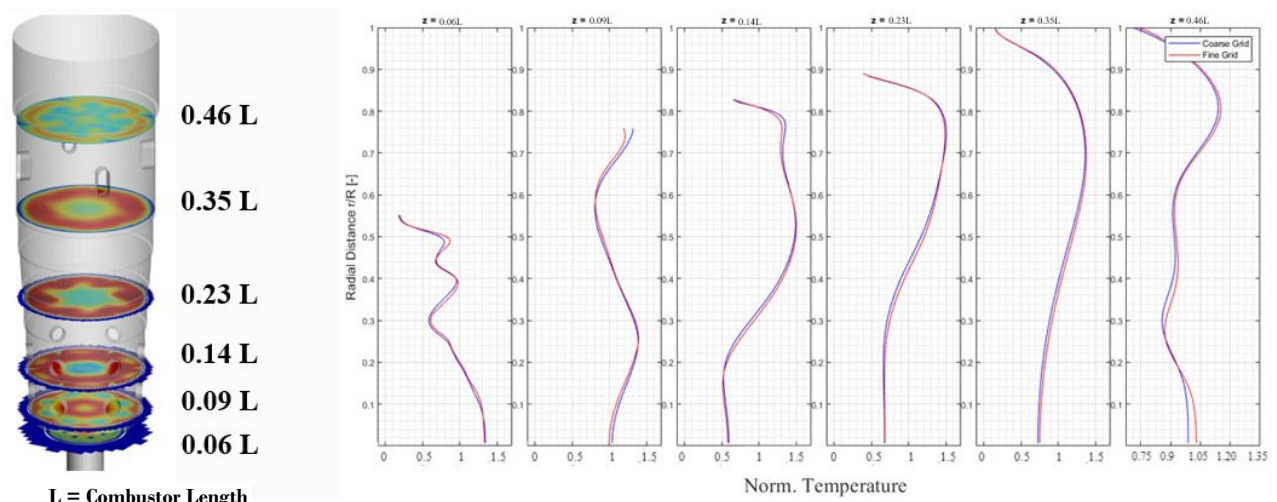


Figure 3. Base and refined mesh comparison.

The figure clearly shows that a higher level of embedding is used in the refined ($n = 5$ vs. $n = 4$). However, thanks to an extended AMR activation, the base grid can reach almost the same level of detail, as it is required by the flow field complexity, resulting in an overall lower computational cost. Even though higher refinement levels have been allowed in the refined mesh, they are triggered only in small zones, such as the injection zone and near-wall regions, which correspond to the inflowing air.

The temperature and velocity profiles against the radial position are represented in Figures 4 and 5, for different axial positions along the combustor. On the ordinate axis, the normalized radial distance r/R is reported, which corresponds to the distance from the center of the burner normalized on the maximum radius R .



L = Combustor Length

N.B. Contour data are from fine grid.

Figure 4. Normalized temperature mean radial distribution at different axial positions for base and refined grid.

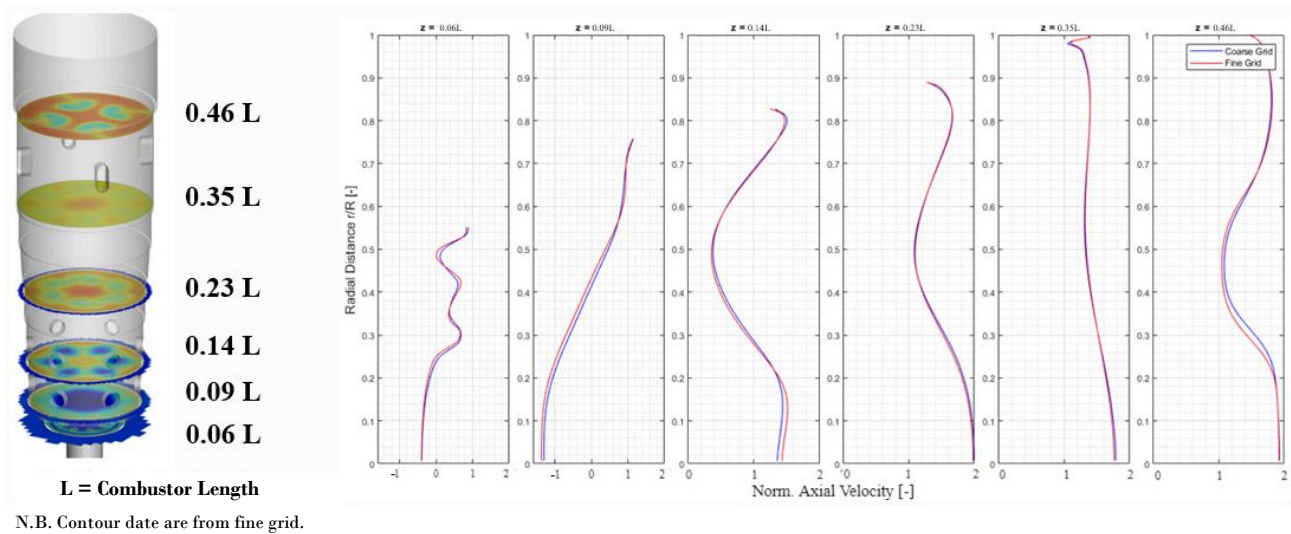


Figure 5. Normalized axial velocity mean radial distribution at different axial positions for base and refined grid.

The velocity and temperature profiles are very close to one another at all of the axial positions. This demonstrates that the base grid returns almost the same results as the refined grid, but with a considerable change in the computational cost (the number of cells is three times larger in the refined case). Therefore, the base grid has been selected for the analyses carried out in this paper.

3.5. Schmidt Number Sensitivity Analysis

In RANS simulations, the Schmidt (Sc) number plays a key role in the definition of the turbulence scalar transfers, in particular in defining the effect of turbulent diffusion over the temperature field and in the system reactivity. A set of experimental studies performed over pipes and boundary layer flows in the last decades suggested that $Sc \approx 0.7$ and for this reason, the default value in CONVERGE is set usually equal to 0.78 [24]. On the other hand, some recent studies suggest conducting a sensitivity analysis over the test case when dealing with an industrial gas turbine application [30], since it could be required to change the Sc value, in accordance with the specific case.

The Sc number sensitivity analysis has been conducted for the TG20 B7/8 turbine at two different operating points. The first is the base load with the operating conditions reported in Table 2. The other operating point will be referred to as 'Duino case' and presents slightly different boundary conditions, as reported in Table 6. The values are normalized with respect to the base load conditions.

Table 6. Base load vs. Duino case boundary conditions.

Boundary Condition	Base Load	Duino Case
Air Mass-Flow Rate	100	99.3
Fuel Flow Rate	100	70
Turbine Pressure	100	97.96
Inlet Air Temperature	100	104.2

The most apparent difference between the cases is the amount of fuel flow rate, indicating a different output power and turbine inlet temperature. For this analysis, an evaluation of the OH concentration maps was selected, which provides an insight into the reactivity of the system and the flame shape.

The maps shown in Figure 6 represent the OH concentration for different turbulent Schmidt numbers in base load conditions. The simulation with $Sc = 0.78$ shows a higher reactivity as compared with the other setups with a lower Sc number.

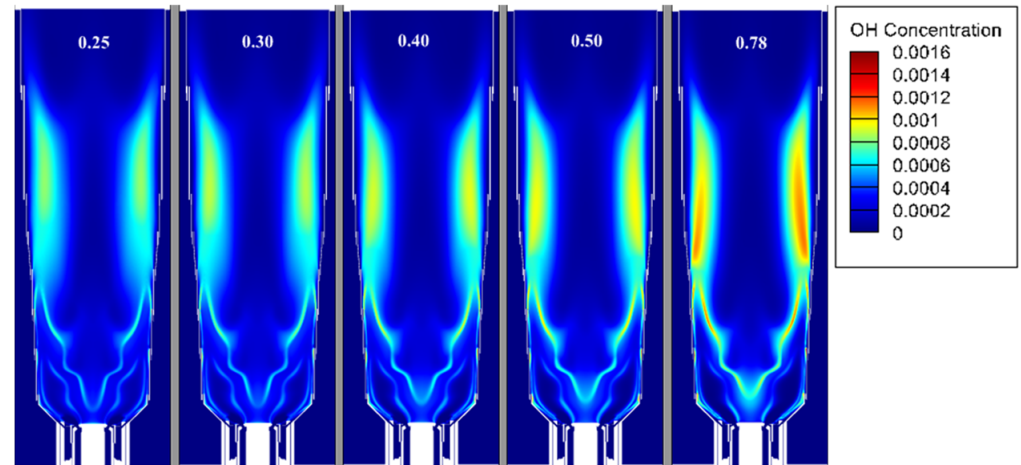


Figure 6. Sensitivity study over the turbulent Schmidt number—base load.

Nevertheless, the results from the Duino case are significantly more sensitive to a change in the turbulent Sc number and are reported in Figure 7. This is due to the lower fuel rate, which determines a reduced fuel-jet speed, and a shorter flame axial development. In the simulation with $Sc = 0.78$, a high reaction zone is present near the injection and suggests the presence of an attached flame. Nevertheless, the simulation with $Sc = 0.5$ shows the lift-off phenomenon, which is the expected behavior. In fact, the visual inspection of the combustor components during maintenance did not reveal flame-related injector damage. As a result, it was possible to exclude the presence of flame shapes, similar to the case with $Sc = 0.78$. For this reason, the Schmidt number was set to 0.5, which is also in agreement with [30].

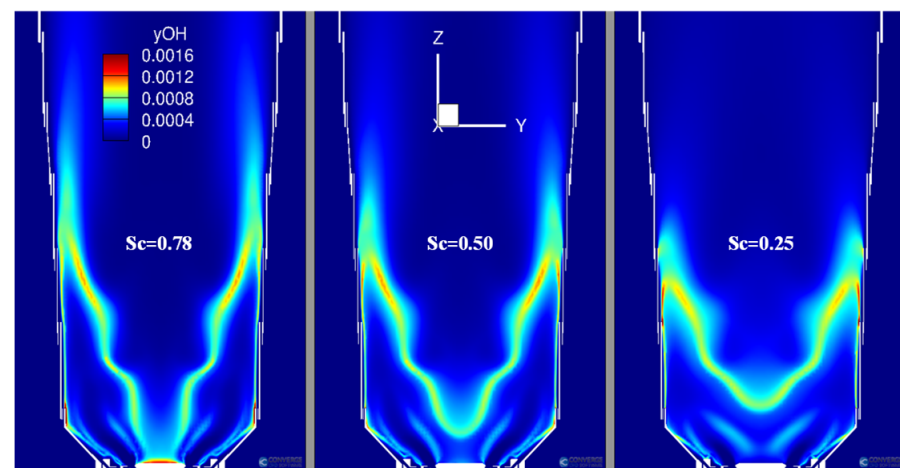


Figure 7. Sensitivity study over the turbulent Schmidt number—Duino case.

4. Results and Discussion

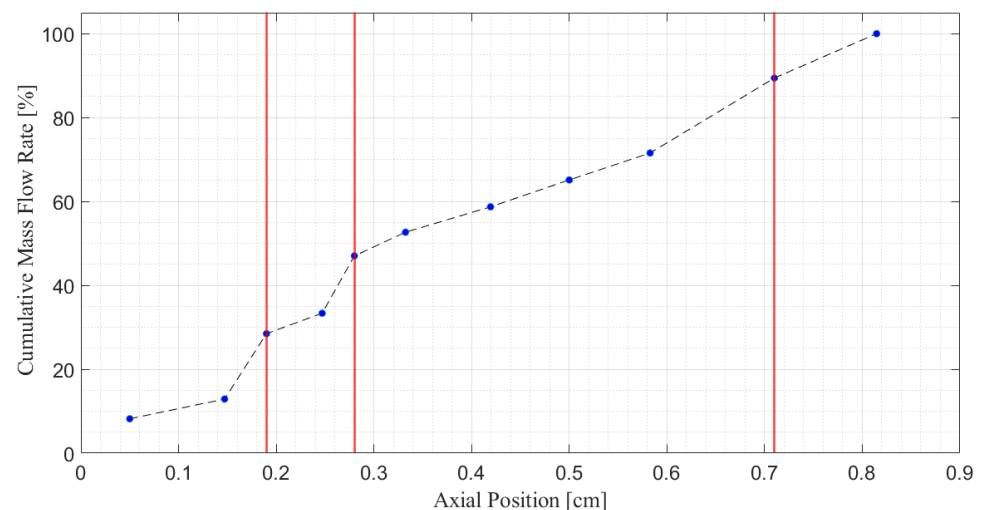
The results of the numerical campaign carried out on the TG20 combustor will be presented hereafter. First, the stability of the converged solution was assessed by checking the standard deviation of the main variables, i.e., the mass-flow rate and the mass-averaged temperature at TP outlet. The values are reported in Table 7.

Table 7. Steady-state solution assessment.

H2 Vol. Fraction [%vol]	St. Dev. Mass-Flow Rate [%]	St. Dev. Temp. [%]
0 (Base Load)	1.15	0.75
15	0.91	0.72
25	1.02	0.72
50	1.02	0.72

Both variables show a standard deviation around 1%, measured with reference to the ‘averaging window’ between 20 and 30 K cycles. All of the values are nearly constant for all the considered blends, thus testifying the suitability of the results for a relative comparison of combustion-related results.

As a starting point, Figure 8 reports the mass-flow rate in each section that is normal to the axis of the basket, as a function of the axial position (normalized). In particular, $x = 0$ corresponds to the injector outlet, whereas $x = 1$ is found at the TP outlet/turbine inlet section. In correspondence to each hole position, the cumulative mass-flow rate is updated by including the hole mass-flow rate, in order that the latter can be obtained through the difference between two consecutive dots. The vertical, red lines in the chart indicate the position of the primary, secondary, and dilution holes.

**Figure 8.** Cumulative mass-flow rate as a function of the axial position in the basket.

As it was recalled in Section 3, the flow split amongst the air holes was part of the problem solution. As shown by the figure, this choice appears as essential for a reliable estimation of the flow patterns inside the basket, as well as of the convective heat transfer toward the basket shell. In fact, the mass-flow rate of the cooling slots represents a remarkable fraction of the overall flow. For example, the total primary plus secondary air flow is around 30% of the overall flow rate, and the one of the cooling slots between the secondary and the dilution holes sum up to around 25%. However, it has been shown that the flow split amongst the holes is virtually not affected by the composition of the fuel, under the working conditions considered in this paper.

Figures 9 and 10 show the mass-averaged profile of the temperature and the axial velocity, respectively, against the axial position, for the different blends. Both quantities have been normalized to their value in the outlet section of TP.

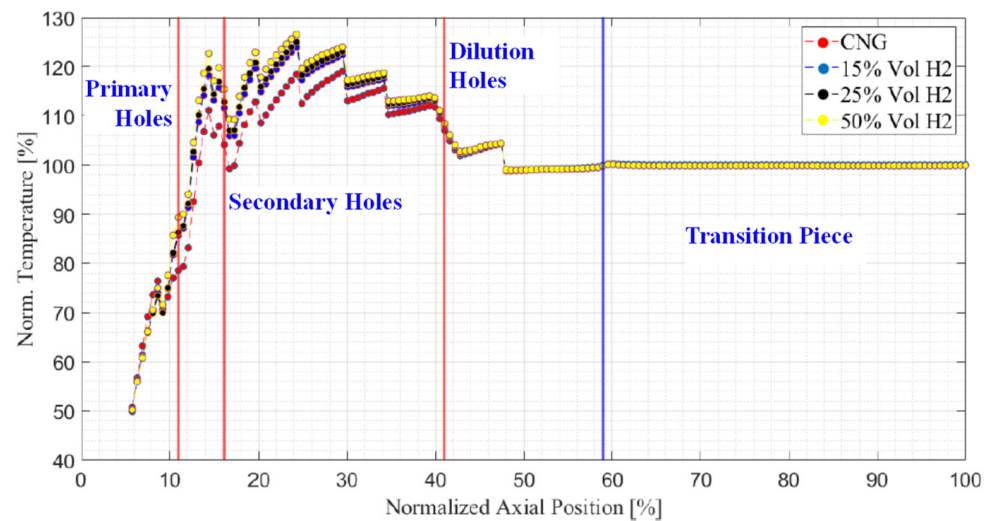


Figure 9. Normalized mass-averaged temperature as a function of the axial position in the basket.

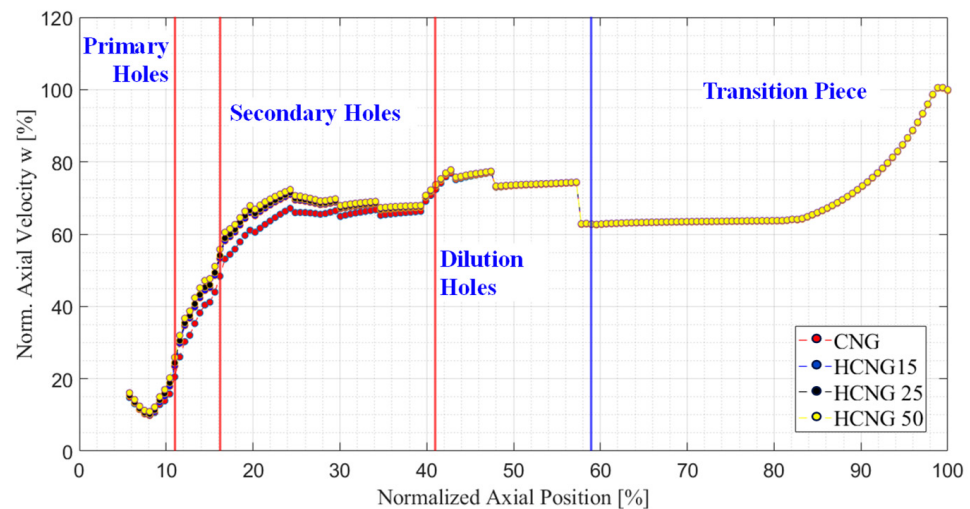


Figure 10. Normalized mass-averaged axial velocity as a function of the axial position in the basket.

In Figure 9, all of the calculated temperatures reach the mass-averaged value of 100, which is a direct consequence of the fuel mass-flow rate imposed, as in Table 3. Moreover, the simulated TIT value for the base load case matches the experimental value almost perfectly, which confirms the correctness of the initial hypothesis of adiabatic flow (Section 3.1). As can be inferred from Figure 9, an increase in the maximum mass-averaged temperature (corresponding to the axial position = 24%) is found for the NG-H₂ blends, which can be quantified between 6 and 8.5% of the normalization value. The increase in the average temperature is clearly visible in the entire region between the secondary and the dilution holes, where most of the oxidation takes place. In that region, a monotonic temperature increase against the hydrogen concentration is also visible, although the dependence is not linear. Accordingly, the decrease in the mixture density determines a virtually proportional increase in the flow velocity, for a given mass-flow rate (Figure 10). This aspect, along with a modified fuel velocity from the nozzles, can affect the flame anchoring, as will be apparent later in this section, as well as the flow turbulence, finally influencing the predicted combustion behavior.

In the following paragraphs, an in-depth analysis of the model results is presented, by referring to a few axial slices as detailed in Figure 11.

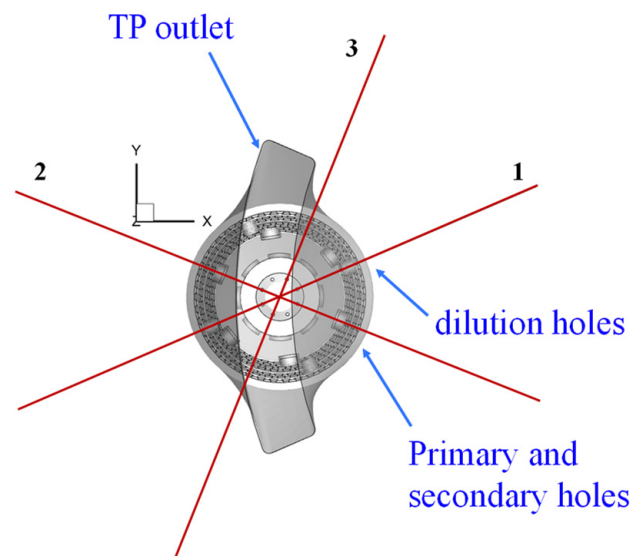


Figure 11. Detail of the section slices for contour visualization. Slice 1 is defined in correspondence to the dilution holes axis. Slice 2 is in phase with the primary and secondary holes. Slice 3 is perpendicular to slice 2 and does not intersect any hole.

The axial velocity contours obtained for the different tests are reported in Figure 12 with reference to slice 2. The general behavior appears to be similar for the different blends, highlighting a few common features. In particular:

- A region with nearly zero axial velocity, in correspondence to the radial inlet flow through the primary and secondary holes;
- a recirculating region in the hollow cone generated by the fuel jets (negative axial component);
- the high-velocity region generated by the decrease in the density in the high-temperature region between the secondary and the dilution holes;
- the nozzle effect in the last part of the TP.

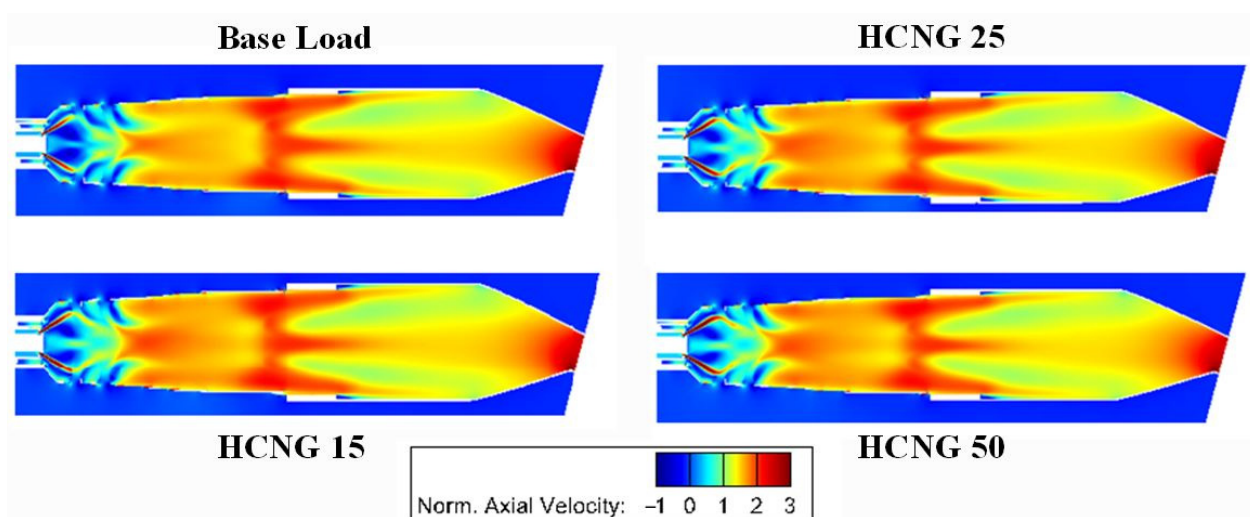


Figure 12. Axial velocity contours in slice 2.

In Figure 12, higher axial velocities are detected in correspondence to the high-temperature regions, as already pointed out in Figure 10. However, the velocity field topology remains almost unchanged for all of the blends. Moreover, the differences tend to quickly vanish downstream of the dilution holes, where the dilution is completed and

the temperature differences amongst the considered blends disappear. Notably, the NG blending with hydrogen leads to an increased fuel velocity within the jets. This is due to the reduced fuel density, which overcomes the reduction of the mass-flow rate, and has an effect on the interaction between the jets and the air entering from the primary holes, as well on the flame anchoring, as will be discussed below. The recirculation pattern underneath the jet tends to be narrower and longer, and interacts more with the primary air in the case of hydrogen, thus inducing a higher velocity of the primary flow.

The increased HCNG jet velocity and the higher bulk flow velocity within the liner, compared with the base load case, also have an impact on the flow turbulence. The model results hint at an increase in the turbulent kinetic energy (TKE) within the fuel jet by about 100%, for the HCNG 50 case with respect to base load. This increment leads to a corresponding increase in the mass-averaged TKE of about 8–9% right upstream of the primary holes (normalized position = 11%, see Figure 10). Downstream of the secondary holes, the turbulence production is sustained by the increased bulk flow velocity. Notably, the increased flow turbulence is reported as beneficial to hydrogen combustion in the literature [31], as it enhances the diffusion of species and enthalpy, finally reducing the increase in the peak temperature and, consequently, NO_x production rates.

Figures 13–15 report the simulated temperature fields (normalized to its value in the outlet section) in the three slices identified above.

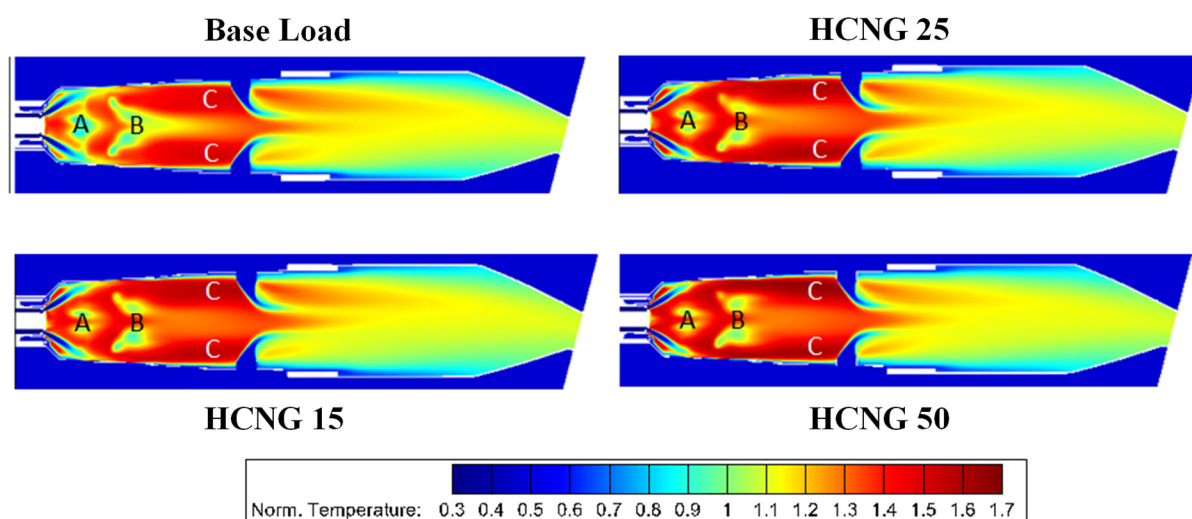


Figure 13. Normalized temperature contours—slice 1. Letters A–C denote specific regions as explained in the text.

The main influence of the hydrogen presence on the combustion process is primarily determined by the higher reactivity and greater $LHV/(A/F)_{st}$ ratio. Both factors lead to an increase in the combustion intensity and flame temperature with respect to the base load case with pure NG. In particular, the overall air-to-fuel ratio is calibrated by targeting the desired TIT and the $LHV/(A/F)_{st}$ ratio can affect the local temperature, considering that most of the diffusive combustion occurs at locally stoichiometric conditions (see the isolines of OH concentration below). Furthermore, the temperature contours in the figures hint at an impact of the aforementioned change in the jet velocity and recirculation zone size on the fuel-air mixing in the primary zone. In particular, the latter effect can be clearly appreciated in slices 1 and 3, where the high-temperature red-colored region is wider and interconnected. The NG-H₂ reactivity also extends inside the recirculation region, with the only exception of the zone around the vortex axes (highlighted with letter A in the figures). The higher $LHV/(A/F)_{st}$ ratio determines the higher temperatures that are visible downstream of the secondary holes exit (B) and in the outer part of the channel between the secondary and dilution holes (C). With specific reference to the temperature differences in region 'C', a comparison between the contour plots shows that they are more evident

than in regions 'A' and 'B', with an increase in both the peak value and width. Accordingly, a more structured dependence of the average temperature profile on the hydrogen content was detected (Figure 9).

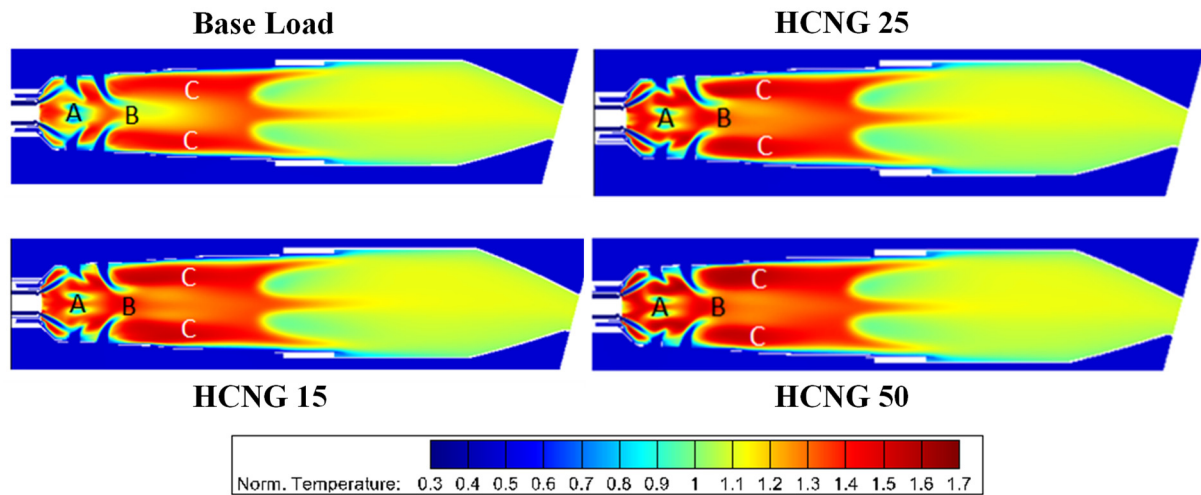


Figure 14. Normalized temperature contours—slice 2. Letters A–C denote specific regions as explained in the text.

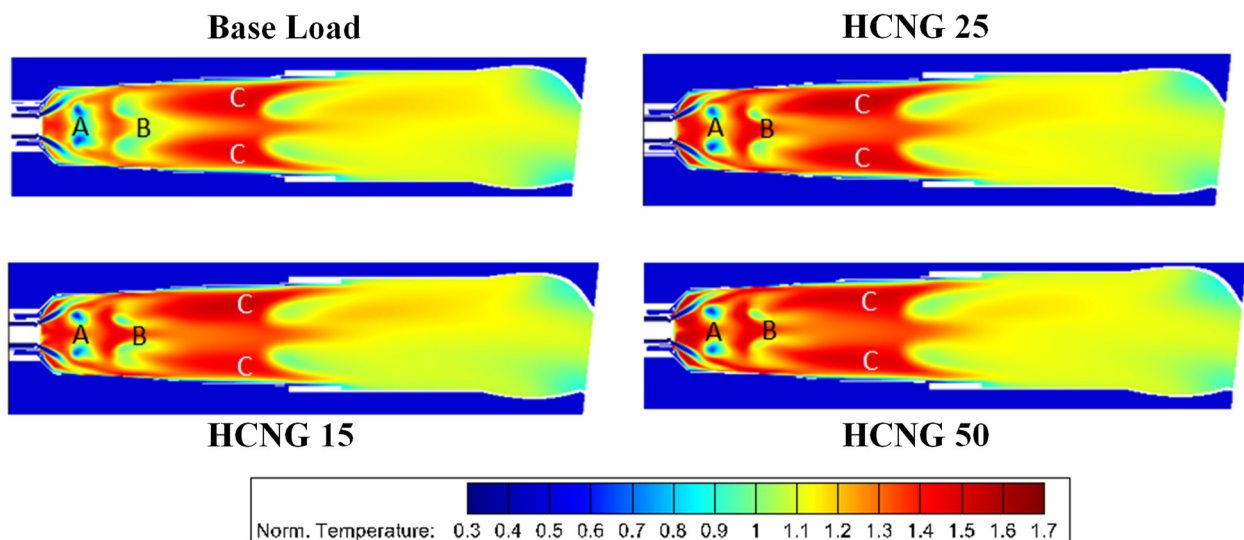


Figure 15. Normalized temperature contours—slice 3. Letters A–C denote specific regions as explained in the text.

Downstream of the dilution holes, the difference between the temperature fields vanishes, since the same TIT has been imposed in the different cases, through the adjustment of the fuel mass-flow rate. Additionally, the temperature profile along the span of the first vane is virtually unchanged, for the considered working conditions, as shown in Figure 16.

Figure 16 reports, on the left picture, the profile of normalized temperature vs. the radial position along the span of the first vane, for the different NG-H₂ blends. A very limited change in the profile can be observed, with a slight decrease in the mid-span value and a slight increase in the temperature at the inner and outlet locations. Accordingly, given that the mass-averaged temperature is maintained at a constant level, the pattern factor (PF) shows a moderate decrease against the hydrogen percentage in the mixture, with the only exception of the case with 15% of H₂ in volume (Figure 17). The PF is defined by [32]:

$$PF = \frac{T_{\max, \text{out}} - T_{\text{mean, out}}}{T_{\text{mean, out}} - T_{\text{in}}} \quad (4)$$

where $T_{\max, \text{out}}$ is the maximum temperature in the outlet TP section, $T_{\text{mean, out}}$ is the mass-averaged temperature in the same section, and T_{in} is the combustor inlet temperature. The pattern factor of the NG case was in line with the available measured data at EthosEnergy, for similar engines. Moreover, the temperature distribution was quite similar to those available at the company (see, for example, [32]). This further supports the reliability and the accuracy of the model presented in this work.

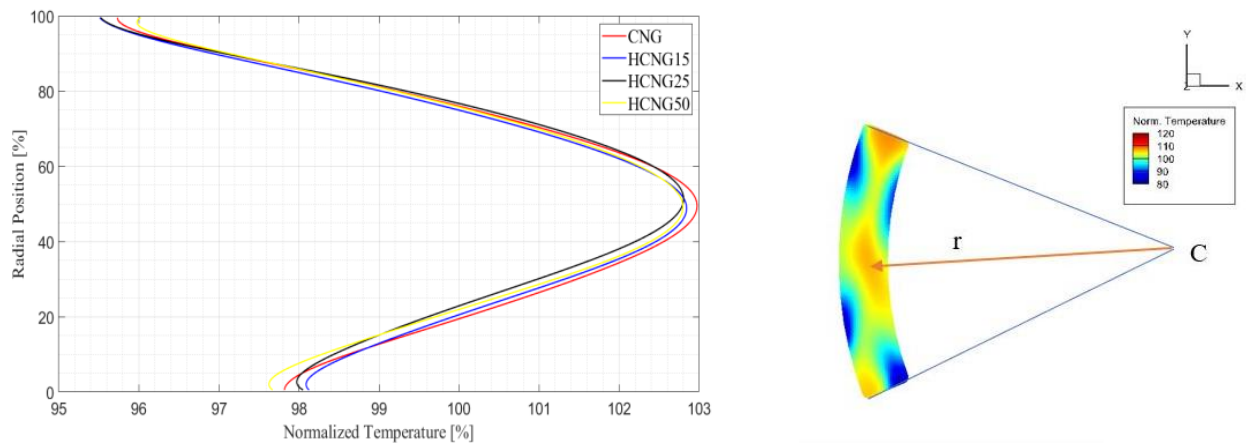


Figure 16. Tangentially-averaged TIT values against radial position (left), and temperature contour in the TP outlet section (right).

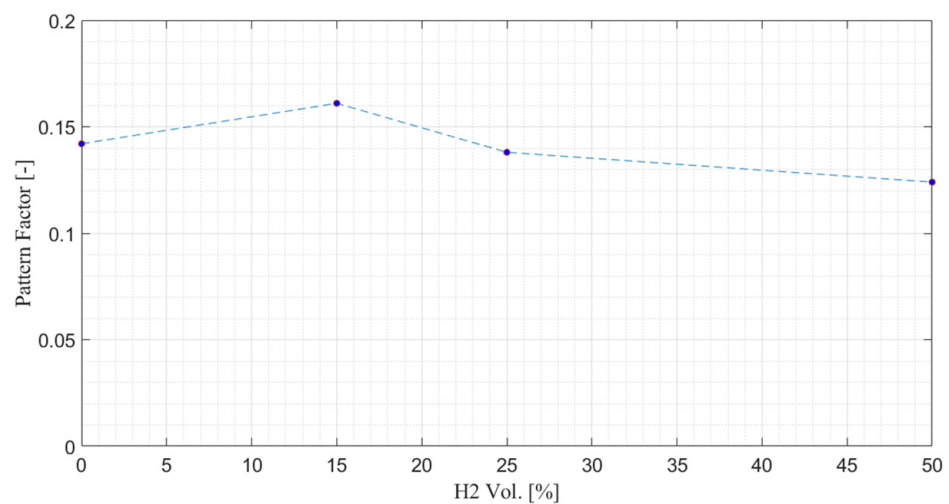


Figure 17. Pattern factor as a function of the fuel hydrogen content.

Figure 18 presents the contours of the OH radical concentration, which has been taken as an indicator of the flame intensity. The close correlation between the OH scalar fields and the temperature in Figure 13 is evident, and demonstrate an increasing reaction intensity as hydrogen is added to NG, particularly in regions 'B' and 'C' (Figures 13–15).

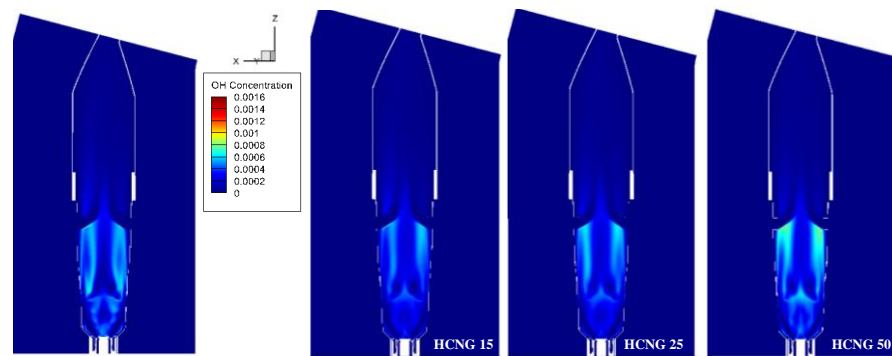


Figure 18. Contours of OH concentration in slice 1.

Figure 19 shows the spatially-resolved temperature increment for the NG-H₂ blends, with respect to the unblended NG.

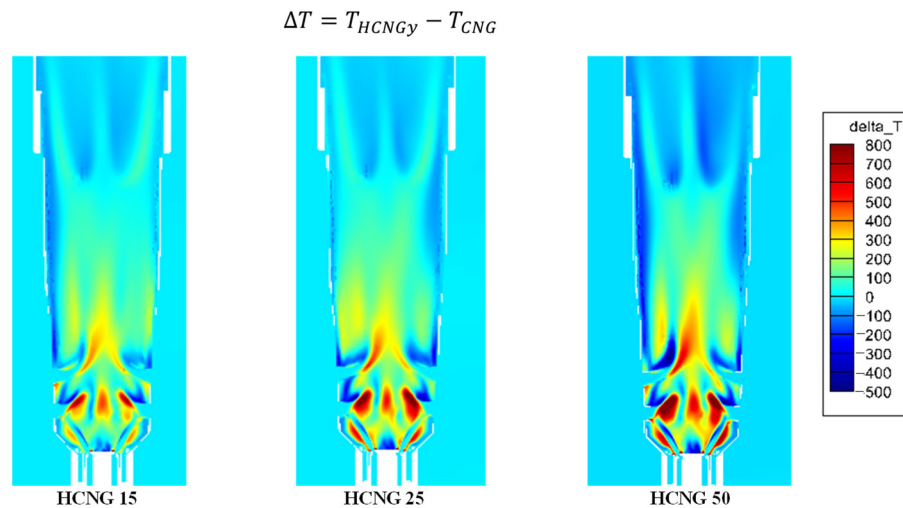


Figure 19. Differential temperature contours for HCNG fueling—slice 2.

As can be seen, a continuous increase in the temperatures can be observed as the H₂ content is increased. For a given H₂ percentage, the highest local increment is observed:

- In the narrow gap between the fuel jet and the lower basket wall;
- in the upper portion of region 'A', where the fuel jet interacts with the primary air flow;
- in region 'B', downstream of the secondary holes position.

The first increment is locally remarkable, but is not spatially wide enough to significantly change the average temperatures in Figure 9. The highest temperature increase is detected in region 'A' and can be quantified as more than 800 K. These temperature increments are accompanied by the presence of oxygen, as can be inferred by the mixture combustion intensity (see the OH concentration results in Figure 18). Consequently, a sensible increase in the NO_x emissions is expected in accordance with the literature, if no countermeasures are taken [10]. Furthermore, the lower distance between the injector and the flame, with the consequent increased thermal stresses on the injector, the swirler, and on the lower basket wall, will require attention for the combustor operation. Both the pollutant emissions and the thermo-mechanical stresses will be the subject of further investigation by the authors, before the effective turbine retrofitting can take place. In particular, the production NG-fueled power unit utilizes water injection to control NO_x emissions. Future work will then be devoted to the estimation of the increment in water content for the HCNG case, which is required to work at constant NO_x emissions. A possible solution aimed at increasing the turbulence inside the basket should also be considered, in accordance with the findings in [31]. The increased temperatures in the proximity of the lower basket wall

and injectors will be used to estimate the increased metal temperature, for a quantitative evaluation of the severity of the new working conditions. On the other hand, of note, the lateral walls of the liner are not expected to suffer from increased operation temperatures, thanks to the effective film cooling effect. The latter is visible in Figures 13–15 as a narrow cold film close to the walls.

Figure 20 shows the concentration contours in slice 2 for the CH₄ and the H₂ fuel species, with reference to the test with 15% of H₂. The figure is helpful in explaining the reason that the most apparent temperature increase was found in the transition from 0 to 15% of hydrogen concentration.

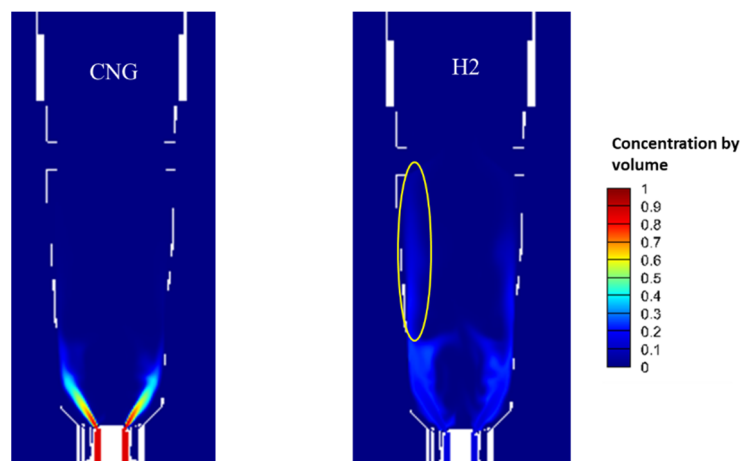


Figure 20. Concentration of NG and H₂ in slice 1—base load CNG vs. 15% H₂ case.

In fact, the CNG is almost entirely consumed near the injection zone, whereas the H₂ is able to reach the dilution holes area, where non-negligible concentrations (10–20% in volume) are detected. This is due to a dramatically different diffusivity, which is almost 40 times higher for hydrogen than for methane (0.2 vs. 7.9 m²/s). For this reason, the higher LHV (2.4 times) determines an increased adiabatic flame temperature, despite the increased (A/F)_{st} ratio (2 times).

5. Conclusions

This work stems from the need to quickly reduce the carbon footprint of the energy production sector, and to analyze the combustion process in a non-premixed gas turbine burner, which is originally designed for CNG fueling, for different hydrogen blends. The analysis was conducted by means of a purposely developed CFD model and aimed at finally retrofitting a 40 MW heavy-duty gas turbine.

The main conclusions were as follows:

- The detailed simulation of the different air flows to the combustor basket, including the cooling flow rate, was fundamental for a correct estimation of the thermal field inside the combustor.
- With reference to the average temperature against the axial position, an increase between 6.5 and 8% was obtained for the NG-H₂ blends, with respect to the unblended CNG operation.
- Higher velocities are also found, as a consequence of the decreased density of combustion products.
- For the original geometry of the liner and injectors, an increased turbulence by around 100% was predicted inside the fuel jets, which determined a rise in the average bulk-flow turbulence of around 8–9%.
- Correspondingly, a local increase in the temperature up to 800 K was obtained, as a combination of the LHV, (A/F)_{st}, and increased diffusivity effects.

- The CNG was found to be almost entirely consumed near the injection zone, whereas non-negligible hydrogen concentrations (10–20% in volume for the HCNG 15 case) could be found downstream of the secondary holes. This contributed to the above-mentioned temperature increase.
- The inspection of OH radical concentration revealed that the flame became more intense as hydrogen was added to the fuel, and overall closer to the injector.
- The latter effect was also determined by a change in the recirculation pattern in the hollow region between the fuel jets, as well as in its interaction with the primary and secondary flows.
- A careful consideration of the NO_x compensation strategies (water injection and/or turbulence optimization) and of the injector and swirler thermal stresses is mandatory before the effective retrofitting can be realized.

Author Contributions: Conceptualization, methodology, software, validation, investigation, data curation, writing—revised draft preparation, writing—review and editing, supervision, S.C.; conceptualization, methodology, software, validation, investigation, data curation, writing—review and editing, supervision, P.G.; conceptualization, methodology, validation, investigation, data curation, writing—revised draft preparation, writing—review and editing, supervision, M.B.; conceptualization, methodology, validation, investigation, data curation, writing—review and editing, supervision, D.A.M.; conceptualization, methodology, validation, investigation, data curation, writing—review and editing, supervision, S.S.; conceptualization, validation, data curation, writing—review and editing, supervision, F.C.; conceptualization, validation, data curation, writing—review and editing, supervision, L.F.; conceptualization, validation, data curation, writing—review and editing, supervision, M.T.; conceptualization, validation, data curation, writing—review and editing, supervision, M.V. All authors have read and agreed to the published version of the manuscript.

Funding: This research received no external funding.

Informed Consent Statement: Not applicable.

Data Availability Statement: Not applicable.

Acknowledgments: The authors would like to thank Scott Drennan, Suresh Nambully, Gabriel Jacobson, Matteo D’Elia and Jyothish Venkataramanan of Convergent Science for their technical support. The contribution of Elisabetta Casto of EthosEnergy Italia to the management of the research project is also acknowledged.

Conflicts of Interest: The authors declare no conflict of interest.

References

1. *Energy Technology Perspectives 2020*; International Energy Agency: Paris, France, 2020.
2. Zeldovich, Y.B. To the Question of Energy Use of Detonation Combustion. *J. Propuls. Power* **2006**, *22*, 588–592. [[CrossRef](#)]
3. Stathopoulos, P. Comprehensive Thermodynamic Analysis of the Humphrey Cycle for Gas Turbines with Pressure Gain Combustion. *Energies* **2018**, *11*, 3521. [[CrossRef](#)]
4. Laveneziana, L.; Rosafio, N.; Salvadori, S.; Misul, D.A.; Baratta, M.; Forno, L.; Valsania, M.; Toppino, M. Conjugate Heat Transfer Analysis of the Aero-Thermal Impact of Different Feeding Geometries for Internal Cooling in Lifetime Extension Processes for Heavy-Duty Gas Turbines. *Energies* **2022**, *15*, 3022. [[CrossRef](#)]
5. Campbell, A.; Goldmeer, J.; Healy, T.; Washam, R.; Molie’re, M.; Citeno, J. Heavy Duty Gas Turbines Fuel Flexibility. In Proceedings of the Turbo Expo: Power for Land, Sea, and Air, Berlin, Germany, 9–13 June 2008; pp. 1077–1085. [[CrossRef](#)]
6. Xing, C.; Chen, X.; Qiu, P.; Liu, L.; Yu, X.; Zhao, Y.; Zhang, L.; Liu, J.; Hu, Q. Effect of fuel flexibility on combustion performance of a micro-mixing gas turbine combustor at different fuel temperatures. *J. Energy Inst.* **2022**, *102*, 100–117. [[CrossRef](#)]
7. Benaissa, S.; Adouane, B.; Ali, S.; Rashwan, S.S.; Aouachria, Z. Investigation on combustion characteristics and emissions of biogas/hydrogen blends in gas turbine combustors. *Therm. Sci. Eng. Prog.* **2021**, *27*, 101178. [[CrossRef](#)]
8. Wu, Y.; Hua, J. Investigating a Retrofit Thermal Power Plant from a Sustainable Environment Perspective—A Fuel Lifecycle Assessment Case Study. *Sustainability* **2022**, *14*, 4556. [[CrossRef](#)]
9. Ricci, M.; Mosele, S.G.; Benvenuto, M.; Astrua, P.; Pacciani, R.; Marconcini, M. Retrofittable Solutions Capability for Gas Turbine Compressors. *Int. J. Turbomach. Propuls. Power* **2022**, *7*, 3. [[CrossRef](#)]
10. Chiesa, P.; Lozza, G.; Mazzocchi, L. Using Hydrogen as Gas Turbine Fuel. *J. Eng. Gas Turbines Power* **2005**, *127*, 73–80. [[CrossRef](#)]
11. Rohani, B.; Saqr, K.M. Effects of hydrogen addition on the structure and pollutant emissions of a turbulent unconfined swirling flame. *Int. Commun. Heat Mass Transf.* **2012**, *39*, 681–688. [[CrossRef](#)]

12. Kashir, B.; Tabejamaat, S.; Jalalatian, N. On large eddy simulation of blended CH₄–H₂ swirling inverse diffusion flames: The impact of hydrogen concentration on thermal and emission characteristics. *Int. J. Hydrogen Energy* **2015**, *40*, 15732–15748. [[CrossRef](#)]
13. European Turbine Network. *ETN Hydrogen Gas Turbines Report*; European Turbine Network: Saint-Gilles, Belgium, 2020.
14. Ebi, D.; Bombach, R.; Jansohn, P. Swirl flame boundary layer flashback at elevated pressure: Modes of propagation and effect of hydrogen addition. *Proc. Combust. Inst.* **2020**, *38*, 6345–6353. [[CrossRef](#)]
15. Marini, A.; Riccio, G.; Martelli, F.; Sigali, S.; Cocchi, S. Numerical Re-Design of a Heavy Duty Gas Turbine Hydro-gen-Fired Combustion Chamber. In Proceedings of the Turbo Expo: Power for Land, Sea, and Air 2010, Glasgow, UK, 14–18 June 2010; Volume 2, pp. 747–757.
16. Brunetti, I.; Riccio, G.; Rossi, N.; Cappelletti, A.; Bonelli, L.; Marini, A.; Paganini, E.; Martelli, F. Experimental and Numerical Characterization of Lean Hydrogen Combustion in a Premixed Burner Prototype. In Proceedings of the ASME 2011 Turbo Expo: Turbine Technical Conference and Exposition 2011, Vancouver, BC, Canada, 6–10 June 2011; Volume 2, pp. 601–612.
17. Therkelsen, P.; Mauzey, J.; McDonnell, V.; Samuelsen, S. Evaluation of a Low Emission Gas Turbine Operated on Hydrogen. In Proceedings of the ASME Turbo Expo 2006, Barcelona, Spain, 8–11 May 2006; Volume 1, pp. 557–564.
18. Cappelletti, A.; Martelli, F. Investigation of a pure hydrogen fueled gas turbine burner. *Int. J. Hydrogen Energy* **2017**, *42*, 10513–10523. [[CrossRef](#)]
19. Funke, H.H.W.; Keinz, J.; Kusterer, K.; Ayed, A.H.; Kazari, M.; Kitajima, J.; Horikawa, A.; Okada, K. Experimental and Numerical Study on Optimizing the Dry Low NO_x Micromix Hydrogen Combustion Principle for Industrial Gas Turbine Applications. *J. Therm. Sci. Eng. Appl.* **2016**, *9*, 021001. [[CrossRef](#)]
20. Nam, J.; Lee, Y.; Joo, S.; Yoon, Y.; Yoh, J.J. Numerical analysis of the effect of the hydrogen composition on a partially premixed gas turbine combustor. *Int. J. Hydrogen Energy* **2019**, *44*, 6278–6286. [[CrossRef](#)]
21. Baratta, M.; Cardile, F.; Misul, D.A.; Rosafio NSalvadori, S.; Forno, L.; Toppino, M. Redesign of the TG20 Heavy-Duty Gas Turbine to Increase Turbine Inlet Temperature and Global Efficiency. In Proceedings of the ASME Turbo Expo 2020, Online, 21–25 September 2020.
22. Pampaloni, D.; Nassini, P.C.; Andreini, A.; Facchini, B.; Cerutti, M. Numerical Investigations of Pollutant Emissions from Novel Heavy-Duty Gas Turbine Burners Operated with Natural Gas. *J. Eng. Gas Turbines Power* **2020**, *142*, 031025. [[CrossRef](#)]
23. Zhang, J.; Sun, Y.; Li, J.; He, X. Study on the Hybrid Cooling of the Flame Tube in a Small Triple-Swirl Combustor. *Energies* **2020**, *13*, 5554. [[CrossRef](#)]
24. Richards, K.J.; Senecal, P.K.; Pomraning, E. *CONVERGE 3.0*; Convergent Science: Madison, WI, USA, 2021.
25. Di Mauro, A.; Ravetto, M.; Goel, P.; Baratta, M.; Misul, D.; Salvadori, S.; Rothbauer, R.; Gretter, R. Modelling Aspects in the Simulation of the Diffusive Flame in A Bluff-Body Geometry. *Energies* **2021**, *14*, 2992. [[CrossRef](#)]
26. Yakhot, V.; Orszag, S.A.; Thangam, S.; Gatski, T.B.; Speziale, C.G. Development of turbulence models for shear flows by a double expansion technique. *Phys. Fluids A Fluid Dyn.* **1992**, *4*, 1510–1520. [[CrossRef](#)]
27. Patil, S.; Abraham, S.; Tafti, D.; Ekkad, S.; Kim, Y.; Dutta, P.; Moon, H.K.; Srinivasan, R. Experimental and Numerical Investigation of Convective Heat Transfer in a Gas Turbine Can Combustor. *ASME J. Turbomach.* **2011**, *133*, 011028. [[CrossRef](#)]
28. Kahraman, N.; Tangöz, S.; Akansu, S.O. Numerical analysis of a gas turbine combustor fueled by hydrogen in comparison with jet-A fuel. *Fuel* **2017**, *217*, 66–77. [[CrossRef](#)]
29. Van Oijen, J.A.; de Goey, L.P.H. Modelling of premixed laminar flames using Flamelet-Generated Manifolds. *Combust. Sci. Technol.* **2000**, *161*, 113–137. [[CrossRef](#)]
30. Jiang, L.Y.; Campbell, I. Prandtl/Schmidt number effect on temperature distribution in a generic combustor. *Int. J. Therm. Sci.* **2009**, *48*, 322–330. [[CrossRef](#)]
31. Hashemi, S.; Fattahi, A.; Sheikhzadeh, G.; Mehrabian, M. Investigation of the effect of air turbulence intensity on NO_x emission in non-premixed hydrogen and hydrogen-hydrocarbon composite fuel combustion. *Int. J. Hydrogen Energy* **2011**, *36*, 10159–10168. [[CrossRef](#)]
32. Gianola, M. Full-Engine Field Test: An Approach to Improve the Gas Turbine Combustion System. *J. Eng. Gas Turbines Power* **1988**, *110*, 677–685. [[CrossRef](#)]